

# Contents

<b>1</b>	<b>Introduction and Theory Overview</b>	<b>1</b>
1.1	Introduction . . . . .	1
1.2	Theory Overview . . . . .	2
1.2.1	Heavy Vector Triplet Model . . . . .	2
1.2.2	Basic Phenomenology . . . . .	3
1.2.3	Explicit Models . . . . .	8
<b>2</b>	<b>The LHC and the CMS Detector</b>	<b>11</b>
2.1	Large Hadron Collider . . . . .	11
2.2	Compact Muon Solenoid . . . . .	13
2.2.1	Tracker . . . . .	15
2.2.2	ECAL . . . . .	16
2.2.3	HCAL . . . . .	17
2.2.4	Muon Chamber . . . . .	19
2.2.5	Trigger System . . . . .	20
<b>3</b>	<b>Analysis Procedures</b>	<b>22</b>
3.1	Monte Carlo Samples and Data sets . . . . .	22
3.1.1	Signal MC . . . . .	22
3.1.2	Background MC . . . . .	24
3.1.3	Data Samples . . . . .	24
3.2	Trigger . . . . .	25
3.3	Physics Objects . . . . .	26

3.3.1	Muon	26
3.3.2	Electron	29
3.3.3	Jet	33
3.3.4	Jet Grooming Algorithms and Pruned Jet Mass	35

# List of Figures

1-1	Branching ratios as a function of the resonance mass for the HVT benchmark model A(left) and model B(right). . . . .	10
1-2	Theoretical production cross-section as a function of new resonance particles for HVT model B benchmark. Dash lines are 8 TeV predictions while solid lines are 13 TeV predictions. . . . .	10
2-1	Overview of the LHC and relative location of the detectors. . . . .	12
2-2	CERN accelerator complex. . . . .	13
2-3	Structure overview of the CMS detector. . . . .	14
2-4	Schematic layout of tracker. . . . .	15
2-5	The pixel detector inside tracker. . . . .	15
2-6	Schematic layout of the CMS ECAL. . . . .	17
2-7	Longitudinal view of one quarter of CMS and the location of HB (hadron barrel calorimeter), HE (hadron endcap calorimeter), HF (hadron forward calorimeter) and HO (hadron outer calorimeter) . . . . .	18
2-8	Slice view of one quarter of muon chamber system. . . . .	20
2-9	CMS triggering and data acquisition architecture. . . . .	21
3-1	Feynman diagram for $Z' \rightarrow Zh \rightarrow 2l2q$ . . . . .	23
3-2	Example of the $E_{2\times 5}/E_{5\times 5}$ computation in the ECAL crystals. $E_{i\times j}$ is the energy contained in a $i \times j$ block around the seed crystal (defined as the highest deposit of the energy of the cluster). . . . .	32

# List of Tables

3.1	Signal samples used in the analysis. . . . .	23
3.2	Background samples used in the analysis. . . . .	24
3.3	Data sets used in this analysis. . . . .	25
3.4	Summary of the muon ID selection criteria. . . . .	28
3.5	Summary of the modified HEEPv4.1 electron ID. . . . .	32

# <sup>1</sup> Chapter 1

## <sup>2</sup> Introduction and Theory Overview

### <sup>3</sup> 1.1 Introduction

<sup>4</sup> This thesis presents the analysis details and the results of the search for heavy reso-  
<sup>5</sup> nances decaying into a  $Z$  boson and a Higgs boson ( $h$ ) at the center-of-mass energy of  
<sup>6</sup> 8 TeV, using  $19.7 \text{ fb}^{-1}$  p-p collision data. In turn, the  $Z$  boson is identified through  
<sup>7</sup> its leptonic decays (leptons often refer to  $e$  and  $\mu$  only in experiments.  $l = e, \mu$ ). The  
<sup>8</sup> Higgs boson  $h$  is expected to hadronically decay into a pair of b-quarks. The investi-  
<sup>9</sup> gated final states consist of two charged leptons which are identified in the detector  
<sup>10</sup> and limit the presence of the background, and two b-quarks from the hadronic Higgs  
<sup>11</sup> decay which collects the largest possible fraction of Higgs events.

<sup>12</sup> This thesis is organised as follows. In the latter part of this chapter, the model that  
<sup>13</sup> predicts heavy resonances is introduced, including the expected cross section and the  
<sup>14</sup> specification of model parameters. In chapter 2, the LHC and the CMS experiment  
<sup>15</sup> are described, including the information of each sub-detector and the trigger system  
<sup>16</sup> of the CMS. The details of the analysis are shown in chapter 3. This chapter reveals  
<sup>17</sup> the way to reconstruct physical objects in CMS. By adding some proper kinematic  
<sup>18</sup> selections on those physics objects, the interested events in data collected by the CMS  
<sup>19</sup> detector can be selected. Moreover, this chapter shows the comparison between data  
<sup>20</sup> and simulation. In the last chapter, the results of the search and the conclusion are  
<sup>21</sup> presented.

## 22 1.2 Theory Overview

23 Although the Higgs boson discovered by the ATLAS and CMS collaborations [1–3]  
 24 imposes strong constraints on theories beyond the Standard Model(SM), the extreme  
 25 fine tuning in quantum corrections required to have a light fundamental Higgs boson  
 26 with mass close to 125 GeV [4–7] suggests that the Standard Model may be incom-  
 27 plete, and not valid beyond a scale of a few TeV. Various dynamical electroweak  
 28 symmetry breaking scenarios which attempt to solve this naturalness problem, such  
 29 as Minimal Walking Technicolor [8], Little Higgs [9–11], or composite Higgs mod-  
 30 els [12–14] predict the existence of new resonances decaying to a vector boson plus a  
 31 Higgs boson.

### 32 1.2.1 Heavy Vector Triplet Model

33 Resonance searches are typically not sensitive to all the details and the free parameters  
 34 of the underlying model, but only to those parameters or combinations of parameters  
 35 that control the mass of the resonance and the interactions involved in its production  
 36 and decay. Therefore, one can employ a simplified description of the resonance de-  
 37 fined by a phenomenological Lagrangian where only the relevant couplings and mass  
 38 parameters are retained. This model-independent strategy applies a Heavy Vector  
 39 Triplet (HVT) [15] to the Standard Model group and reproduces a large class of ex-  
 40 plicit models. In Eq. (1.1), the mathematical form of the simplified Lagrangian is  
 41 defined, where  $V_\nu^a$ ,  $a = 1,2,3$ , is a real vector with vanishing hypercharge in the ad-  
 42 joint representation of  $SU(2)_L$ , it describes one charged and one neutral heavy spin-1  
 43 particle with charge eigenstate fields, and  $D_{[\mu} V_{\nu]}^a$  represents the covariant derivative.

$$\begin{aligned} \mathcal{L}_V = & -\frac{1}{4} D_{[\mu} V_{\nu]}^a D^{[\mu} V^{\nu]}_a + \frac{m_V^2}{2} V_\mu^a V^{\mu a} \\ & + ig_V c_H V_\mu^a H^\dagger \tau^a \overset{\leftrightarrow}{D}^\mu H + \frac{g^2}{g_V} c_F V_\mu^a \sum_f \bar{f}_L \gamma^\mu \tau^a f_L \\ & + \frac{g_V}{2} c_{VVV} \epsilon_{abc} V_\mu^a V_\nu^b D^{[\mu} V^{\nu]}_c + \text{quadrilinear terms} \end{aligned} \quad (1.1)$$

$$V_\mu^\pm = \frac{V_\mu^1 \mp i V_\mu^2}{\sqrt{2}}, \quad V_\mu^0 = V_\mu^3 \quad (1.2)$$

$$D_{[\mu} V_{\nu]}^a = D_\mu V_\nu^a - D_\nu V_\mu^a, \quad D_\mu V_\nu^a = \partial_\mu V_\nu^a + g \epsilon^{abc} W_\mu^b V_\nu^c \quad (1.3)$$

$$H = \begin{pmatrix} \phi^+ \\ \phi^- \end{pmatrix} = \begin{pmatrix} \frac{1}{\sqrt{2}}(\phi_1 + i\phi_2) \\ \frac{1}{\sqrt{2}}(\phi_3 + i\phi_4) \end{pmatrix} \quad (1.4)$$

<sup>44</sup>

<sup>45</sup> In these models, new heavy vector bosons ( $V^\pm, V^0$ ) that couple to the SM Higgs  
<sup>46</sup> doublet (Eq. 1.4) and SM gauge bosons with the parameters  $c_H$  and  $g_V$  and to the  
<sup>47</sup> fermions via the combination  $(g^2/g_V)c_F$ . The parameter  $g_V$  represents the strength  
<sup>48</sup> of the new vector boson interaction, while  $c_H$  and  $c_F$  represent the couplings to the  
<sup>49</sup> Higgs and the fermions respectively, and are expected to be of the order of unity in  
<sup>50</sup> most models.

### <sup>51</sup> 1.2.2 Basic Phenomenology

#### <sup>52</sup> Masses and Mixings

After electro-weak symmetry breaking (EWSB), the only massless state is photon, which can be identified as the gauge field associated with the unbroken  $U(1)_{em}$ . The two other neutral mass eigenstates are the SM  $Z$  boson and one heavy vector of mass  $M_0$  which are obtained by diagonalizing the mass matrix of the  $(Z, V^0)$  system by a rotation with angle  $\theta_N$

$$\begin{pmatrix} Z \\ V^0 \end{pmatrix} \rightarrow \begin{pmatrix} \cos \theta_N & \sin \theta_N \\ -\sin \theta_N & \cos \theta_N \end{pmatrix} \begin{pmatrix} Z \\ V^0 \end{pmatrix}. \quad (1.5)$$

The mass matrix is

$$\mathcal{M}_N^2 = \begin{pmatrix} \hat{m}_Z^2 & c_H \xi \hat{m}_Z \hat{m}_V \\ c_H \xi \hat{m}_Z \hat{m}_V & \hat{m}_V^2 \end{pmatrix}, \text{ where } \begin{cases} \hat{m}_Z = \frac{e\hat{v}}{2\sin\theta_W \cos\theta_W} \\ \hat{m}_V^2 = m_V^2 + g_V^2 c_{VVHH} \hat{v}^2 \\ \xi = \frac{g_V \hat{v}}{2\hat{m}_V} \end{cases}. \quad (1.6)$$

In the above equations  $\hat{v}$  denotes the Vacuum Expectation Value (VEV) defined by  $\langle H^\dagger H \rangle = \hat{v}^2/2$ , and one should know the masses  $\hat{m}_Z$  and  $\hat{m}_V$  do not coincide with the physical  $Z$  boson and the masses of the new resonances of this model, although they do in the approximations later (Eq. 1.12). The mass eigenvalues and the rotation angles are easily obtained by inverting the relations

$$\begin{aligned} Tr[\mathcal{M}_N^2] &= \hat{m}_Z^2 + \hat{m}_V^2 = m_Z^2 + M_0^2, \\ Det[\mathcal{M}_N^2] &= \hat{m}_Z^2 \hat{m}_V^2 (1 - c_H^2 \xi^2) = m_Z^2 M_0^2, \\ \tan 2\theta_N &= \frac{2c_H \xi \hat{m}_Z \hat{m}_V}{\hat{m}_V^2 - \hat{m}_Z^2}. \end{aligned} \quad (1.7)$$

- <sup>53</sup> Note that  $M_0$  represents the real mass eigenvalue of the neutral heavy vector boson.
- <sup>54</sup> Moreover, since we assume  $\hat{m}_V > \hat{m}_Z$ , the only variable controls the sign of the
- <sup>55</sup> tangent function is  $c_H$ , which is model dependent. Once the sign of  $c_H$  is determined,
- <sup>56</sup> the tangent can be uniquely inverted.

The situation is similar in the charged vector mass matrix of  $(W^\pm, V^\pm)$  system, and  $M_\pm$  denotes the real mass eigenvalue of charged states as well.

$$\mathcal{M}_C^2 = \begin{pmatrix} \hat{m}_W^2 & c_H \xi \hat{m}_W \hat{m}_V \\ c_H \xi \hat{m}_W \hat{m}_V & \hat{m}_V^2 \end{pmatrix}, \text{ where } \hat{m}_W = \frac{e\hat{v}}{2\sin\theta_W} = \cos\theta_W \hat{m}_Z, \quad (1.8)$$

where it is diagonalized by

$$\begin{aligned} Tr[\mathcal{M}_C^2] &= \hat{m}_W^2 + \hat{m}_V^2 = m_W^2 + M_\pm^2 , \\ Det[\mathcal{M}_C^2] &= \hat{m}_W^2 \hat{m}_V^2 (1 - c_H^2 \xi^2) = m_W^2 M_\pm^2 , \\ \tan 2\theta_C &= \frac{2c_H \xi \hat{m}_W \hat{m}_V}{\hat{m}_V^2 - \hat{m}_W^2} . \end{aligned} \quad (1.9)$$

By checking Eq. (1.6) and Eq. (1.8), the charged and neutral mass matrices are connected by custodial symmetry, which can be shown in full generality to imply

$$\mathcal{M}_C^2 = \begin{pmatrix} \cos \theta_W & 0 \\ 0 & 1 \end{pmatrix} \mathcal{M}_N^2 \begin{pmatrix} \cos \theta_W & 0 \\ 0 & 1 \end{pmatrix} . \quad (1.10)$$

By taking the determinant of the above equation, or equivalently by comparing the charged and neutral determinants in Eq. (1.7) and Eq. (1.9), we obtain a generalized custodial relation among the physical masses

$$m_W^2 M_\pm^2 = \cos^2 \theta_W m_Z^2 M_0^2 . \quad (1.11)$$

From the simple formula above, we can start to identify the physically reasonable region of the parameter space in this model. We aim at describing new vectors with masses at or above the TeV scale, but we also want the SM masses  $m_{W,Z} \sim 100$  GeV to be reproduced. Therefore we require a hierarchy in the mass relation of SM  $Z$  and  $W$  bosons versus the new vectors.

$$\frac{\hat{m}_{W,Z}}{\hat{m}_V} \sim \frac{m_{W,Z}}{M_{\pm,0}} \leq 10^{-1} \ll 1 \quad (1.12)$$

Use the limit above, we can expand the determinant formulas both in Eq. (1.7) and Eq. (1.9) to obtain simple approximations for  $m_W$  and  $m_Z$

$$\begin{aligned} m_Z^2 &= \hat{m}_Z^2 (1 - c_H^2 \xi^2) (1 + \mathcal{O}(\hat{m}_Z^2 / \hat{m}_V^2)) , \\ m_W^2 &= \hat{m}_W^2 (1 - c_H^2 \xi^2) (1 + \mathcal{O}(\hat{m}_W^2 / \hat{m}_V^2)) . \end{aligned} \quad (1.13)$$

The parameter  $\xi$  can be either very small or of order unity. Both cases are realized in explicit models. While  $\xi \ll 1$  is the most common situation,  $\xi \sim 1$  only occurs in strongly coupled scenarios at very large  $g_V$ . In these approximations, SM tree-level experimental observation can be reproduced to percent accuracy.

Since  $\hat{m}_W = \cos \theta_W \hat{m}_Z$ , the  $W$ - $Z$  mass ratio is thus given by

$$\frac{m_W^2}{m_Z^2} \simeq \cos^2 \theta_W . \quad (1.14)$$

Eq. (1.14) has one important implication on the masses of the new vectors. When combined with the custodial relation Eq. (1.11), it tells us that the charged and neutral  $V$ s are practically degenerate

$$M_{\pm}^2 = M_0^2(1 + \mathcal{O}(\%)) , \quad (1.15)$$

<sup>57</sup> In the following, when working at the leading order in the limit Eq. (1.12), we can  
<sup>58</sup> ignore the mass splitting and denote the mass of the charged and the neutral states  
<sup>59</sup> collectively as  $M_V$ . It is easy to check that in that limit  $M_V = \hat{m}_V$ .

## <sup>60</sup> Decay Widths

Because of the hierarchy in the mass matrices, the mixing angles are naturally small. By looking at Eqs. (1.7), (1.9) and (1.12) we can estimate

$$\theta_{N,C} \simeq c_H \xi \frac{\hat{m}_{W,Z}}{\hat{m}_V} \leq 10^{-1} , \quad (1.16)$$

and after rotating to the mass basis, the coupling of the neutral and charged resonances to left- and right-handed fermion chiralities can be written in a compact form

for each fermion species  $F = \{l, q, 3\}$ .

$$\begin{cases} g_L^N = \frac{g^2}{g_V} \frac{c_F}{2} \cos \theta_C + (g_L^Z)_{SM} \sin \theta_N \simeq \frac{g^2}{g_V} \frac{c_F}{2} , \\ g_R^N = (g_R^Z)_{SM} \sin \theta_N \simeq 0 \\ g_L^C = \frac{g^2}{g_V} \frac{c_F}{2} \cos \theta_C + (g_L^W)_{SM} \sin \theta_C \simeq \frac{g^2}{g_V} \frac{c_F}{2} , \\ g_R^C = 0 \end{cases} \quad (1.17)$$

In the above equation  $(g_{L,R}^{W,Z})_{SM}$  denote the ordinary SM  $W$  and  $Z$  couplings (with the normalization given by  $g_L^W = g/\sqrt{2}$ ).

Given that the rotation angles are small, the couplings further simplify, as also shown in the equation. We could see that  $V$  interact mainly with left-handed chiralities and that all the couplings for each fermion species are controlled by the parameter combination  $g^2/g_V c_F$ . This gives tight correlations among different channels

$$\Gamma_{V_\pm \rightarrow f\bar{f}} \simeq 2\Gamma_{V_0 \rightarrow f\bar{f}} \simeq N_C[f] \left(\frac{g^2 c_F}{g_V}\right)^2 \frac{M_V}{48\pi}, \quad (1.18)$$

where  $N_C[f]$  is the number of colors (3 for the di-quark and 1 for the dilepton decays). The parameters  $c_F = \{c_l, c_q, c_3\}$  control the relative BRs to leptons, light quarks and the third family.

In the case of di-boson decay width

$$\begin{aligned} \Gamma_{V_0 \rightarrow W_L^+ W_L^-} &\simeq \Gamma_{V_\pm \rightarrow W_L^\pm Z_L} \simeq \frac{g_V^2 c_H^2 M_V}{192\pi} \frac{(1 + c_H c_{VVV} \xi^2)^2}{(1 - c_H^2 \xi^2)^2} = \frac{g_V^2 c_H^2 M_V}{192\pi} [1 + \mathcal{O}(\xi^2)], \\ \Gamma_{V_0 \rightarrow Z_L h} &\simeq \Gamma_{V_\pm \rightarrow W_L^\pm h} \simeq \frac{g_V^2 c_H^2 M_V}{192\pi} \frac{(1 - 4c_{VVH} \xi^2)^2}{1 - c_H^2 \xi^2} = \frac{g_V^2 c_H^2 M_V}{192\pi} [1 + \mathcal{O}(\xi^2)]. \end{aligned} \quad (1.19)$$

<sup>61</sup> Note that Eq. (1.19) is derived in the Equivalent Gauge [16] because the decay to transverse SM vectors is highly suppressed while to the longitudinal parts grows with the energy of the process, therefore the Unitary Gauge which is used in the original

<sup>64</sup> Lagrangian is instead useful. The channels that are not shown in the above equations  
<sup>65</sup> are either forbidden or suppressed like the decays to transverse polarizations.

<sup>66</sup> From this section, a very simple picture emerges. At small  $\xi$ , all the decay widths  
<sup>67</sup> are fixed with a given resonance mass  $M_V$  and the couplings  $\{g^2 c_F/g_V, g_V c_H\}$  which  
<sup>68</sup> control the BRs in all relevant channels. Parameters  $c_{VVV}$ ,  $c_{VHH}$  and  $c_{VW}$  are  
<sup>69</sup> basically irrelevant. Thus, the basic phenomenology of this model is well described  
<sup>70</sup> by a good approximation.

### <sup>71</sup> 1.2.3 Explicit Models

Now the general picture is clear, we can get exact values of the widths and BRs from explicit models. Consider two benchmark models, A and B, which correspond to two explicit models describing the heavy vectors in Refs. [17] and [12] respectively. All the  $c$  parameters are fixed to specific values in these models and the only free parameters are the resonance mass  $M_V$  and coupling  $g_V$ . Moreover, model A is inspired by weakly coupled extensions of the SM gauge group while model B is by strongly coupled scenarios of EWSB, *i.e.* Composite Higgs models, we will consider them in different regions of  $g_V$ , relatively small  $g_V \leq 3$  and relatively large  $g_V \geq 3$ .

Figure 1-1 shows the BRs as functions of the mass in model A and B. As expected from the previous discussion and according to Refs. [17], model A predicts

$$c_H \simeq -g^2/g_V^2, c_F \simeq 1, \\ g_V^2 c_H^2 \simeq g^4 c_F^2/g_V^2 \simeq g^2/g_V. \quad (1.20)$$

Therefore Eq. (1.18) and (1.19) can be determined in the following form for  $V_0$  in model A ( $g_V = 1$ ),

$$\Gamma_{V_0 \rightarrow f\bar{f}'} \simeq N_c[f] \frac{g^4 M_V}{96\pi} \\ \Gamma_{V_0 \rightarrow W^+W^-} \simeq \Gamma_{V_0 \rightarrow Zh} \simeq \frac{g^4 M_V}{192\pi}. \quad (1.21)$$

One can easily check either from the plot or the equation, a factor of two difference comparing the BRs between fermions and bosons. Due to the color factor, leptons and quarks also have a difference by a factor of three. Since the  $c_F$  term is universal both in A and B. The total width in model A decreases with increasing  $g_V$  because of the overall suppression ( $g^2/g_V$ ) in Eq. (1.20).

On the contrary, in model B the  $c_H$  term is unsuppressed

$$c_H \simeq c_F \simeq 1 , \\ g_V^2 c_H^2 \simeq g_V^2 , g^2 c_{c_F} / g_{g_V} \simeq g^2 / g_V . \quad (1.22)$$

Thus the determinate  $V_0$  decay widths for model B ( $g_V = 3$ ) are

$$\Gamma_{V_0 \rightarrow f\bar{f}'} \simeq N_c[f] \frac{g^4 M_V}{342\pi} \\ \Gamma_{V_0 \rightarrow W^+W^-} \simeq \Gamma_{V_0 \rightarrow Zh} \simeq \frac{3M_V}{64\pi} . \quad (1.23)$$

- <sup>72</sup> For model B <sub>$g_V=3$</sub>  the dominant BRs are into di-bosons and the fermionic decays are
- <sup>73</sup> extremely suppressed. Moreover, the total width increases with increasing  $g_V$  since it
- <sup>74</sup> is dominated by the di-boson width which grows with  $g_V$  as expected from Eq. (1.22).
- <sup>75</sup> This model B is particularly interesting for the present search, since it predicts signal
- <sup>76</sup> cross sections of the order of fb [15] [18] [Fig. 1-2], branching ratios to vector bosons
- <sup>77</sup> close to unity, and thus being accessible at the LHC. In the latter chapters, the mass
- <sup>78</sup> eigenstate of the neutral heavy vector boson in model B scenario refers to the  $Z'$
- <sup>79</sup> particle, which is the search target of this thesis.

<sup>80</sup>

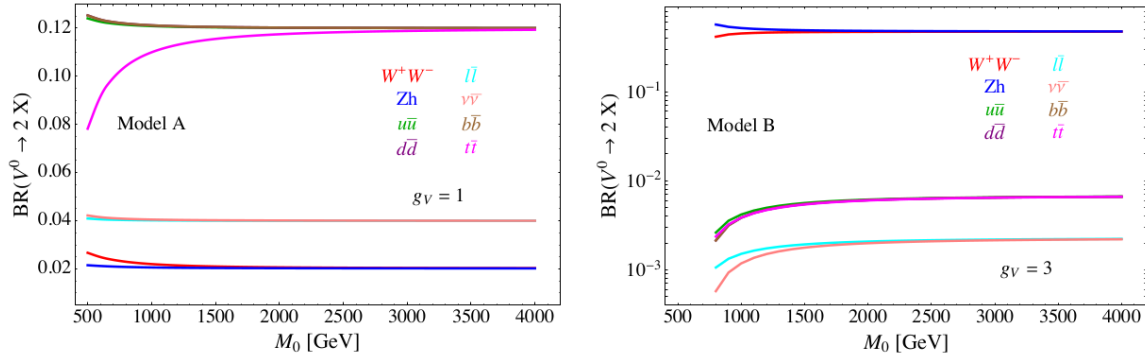


Figure 1-1: Branching ratios as a function of the resonance mass for the HVT benchmark model A(left) and model B(right).

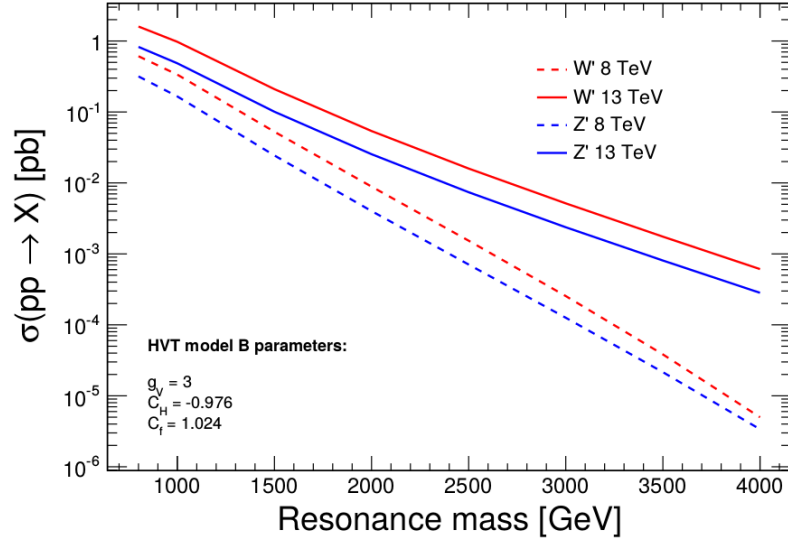


Figure 1-2: Theoretical production cross-section as a function of new resonance particles for HVT model B benchmark. Dash lines are 8 TeV predictions while solid lines are 13 TeV predictions.

81 **Chapter 2**

82 **The LHC and the CMS Detector**

83 This thesis is based on the data collected by the Compact Muon Solenid (CMS)  
84 detector at the Large Hadron Collider (LHC). CMS is one of the two largest detectors  
85 built at the LHC. This chapter will briefly introduce the LHC and the CMS detector.

86 **2.1 Large Hadron Collider**

87 The LHC is the world’s most powerful hadron collider and the largest experimental  
88 facility ever. It was built by the European Organization for Nuclear Research (CERN)  
89 between 1998 and 2008 in collaboration with over 10,000 scientists and engineers from  
90 over 100 countries, as well as hundreds of universities and laboratories. It lies in a  
91 tunnel of 27 km in circumference, as deep as 175 m beneath the France–Switzerland  
92 border near Geneva. The designed maximum collision energy and highest luminosity  
93 of the LHC are 14 TeV and  $10^{-34}\text{cm}^{-2}\text{s}^{-1}$ , respectively.

94 Other accelerators that had been originally built at CERN for previous experi-  
95 ments serve as an injection chain for the LHC now (Fig. 2-2). The proton beam starts  
96 from LINAC, a small linear accelerator, where the energy of protons first reaches at  
97 50 MeV. The proton beam then passes through a booster and goes to the PS, where  
98 it is accelerated up to 25 GeV. After that, it reaches 450 GeV in the SPS. The beam  
99 is finally injected in the LHC ring from the SPS, and it had been accelerated up to  
100 4 TeV in 2012. In early 2015, the proton beam had been accelerated to 6.5 TeV, a

101 value near its designed energy, before undergoing collision.

102 There are four collision points at the LHC, corresponding to four main experiments, CMS, ATLAS, LHCb and ALICE. The ALICE experiment is optimized to  
103 study heavy-ion (Pb-Pb nuclei) collisions and focusing on the physics of strongly  
104 interacting matter at extreme energy densities. LHCb is a specialized b-physics ex-  
105 periment, measuring the parameters of CP violation in the interactions of b-hadrons.  
106 Such studies can help to explain the matter-antimatter asymmetry of the universe.  
107 Last, CMS and ATLAS are two general purpose detectors. The aims of these two  
108 experiments are investigating a wide range of physics, including the search for the  
109 beyond standard model particles, extra dimensions, and dark matter.  
110



Figure 2-1: Overview of the LHC and relative location of the detectors.

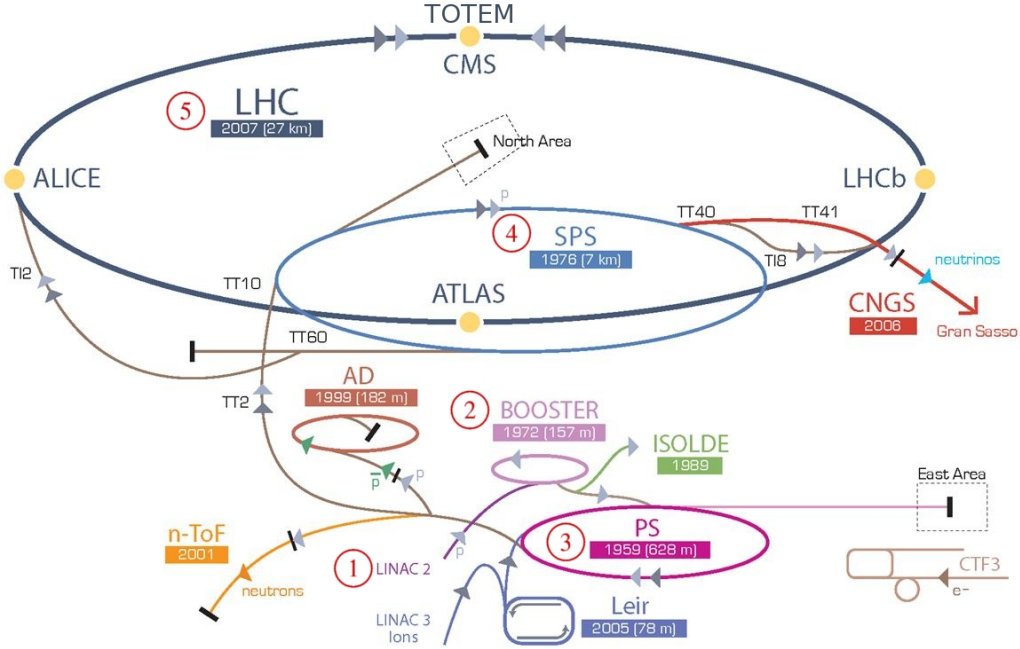


Figure 2-2: CERN accelerator complex.

## 2.2 Compact Muon Solenoid

The Compact Muon Solenoid (CMS) is designed to cope very high rate of interactions expected to take place at the high LHC luminosity. It has the typical structure of detectors at hadron colliders: a central region (*barrel*) enclosed by two disks (*endcaps*). The structure of CMS can be seen in Fig. 2-3.

### Solenoid and Sub-detectors

CMS features a powerful superconducting coil, generating a solenoidal magnetic field around 3.8 Tesla in a large volume which hosts different sub-detectors. The magnetic field lines close through steel yoke in the outer region. The distinct sub-detectors are designed in order to obtain the highest possible resolution and the largest acceptance for every kind of particles.

The innermost layer is a silicon-based tracker. Surrounding it is a scintillating crystal electromagnetic calorimeter (ECAL), which is itself surrounded with a sampling calorimeter for hadrons (HCAL). The tracker and the calorimeters are compact

enough to fit inside the CMS Solenoid. Outside the magnet are the large muon chambers.

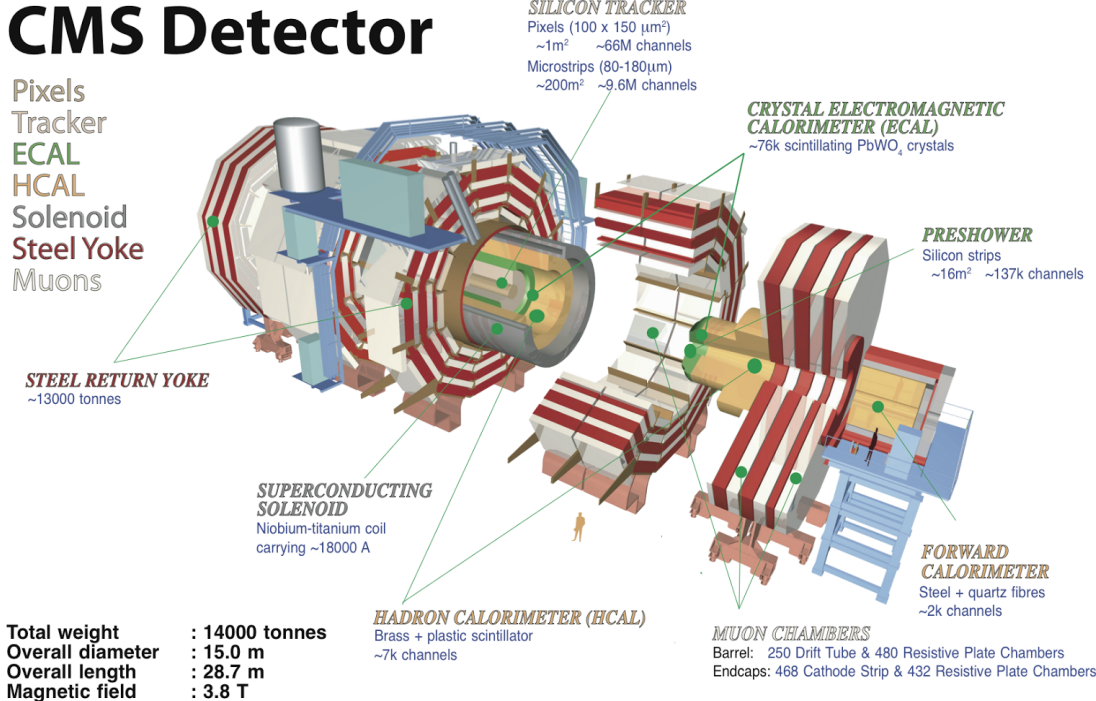


Figure 2-3: Structure overview of the CMS detector.

127 Coordinate System

The CMS coordinate system is oriented such that the  $x$ -axis points to the center of the LHC ring, the  $y$ -axis points vertically upward and the  $z$ -axis is in the direction of the beam. The azimuthal angle  $\phi$  is measured from the  $x$ -axis in the  $x - y$  plane and the radial coordinate in this plane is denoted by  $r$ . The polar angle  $\theta$  is defined in the  $r - z$  plane, while the pseudo-rapidity  $\eta = -\ln \tan(\theta/2)$ . The momentum component transverse to the beam direction, denoted by  $p_T$ , is computed from the  $x$ - and  $y$ -components, and the transverse energy is defined as  $E_T = E \sin \theta$ .

### <sup>135</sup> 2.2.1 Tracker

<sup>136</sup> Tracker is the most inner part of CMS that records the productions of collisions in the  
<sup>137</sup> first place. It traces the charged particles' trajectories. Physicists can reconstruct the  
<sup>138</sup> vertices of the interaction and the momentum of charged particles by linking tracks  
<sup>139</sup> to the collider's pipe and measuring the curves of particles under magnetic field.

<sup>140</sup> The tracking system is composed of two kinds of detector, the pixel detector and  
<sup>141</sup> silicon strip detector. The pixel detector is built from three barrel layers at  $r = 44$ ,  
73, 102 mm, and two endcap disks on each side at  $z = \pm 345, \pm 465$  mm.

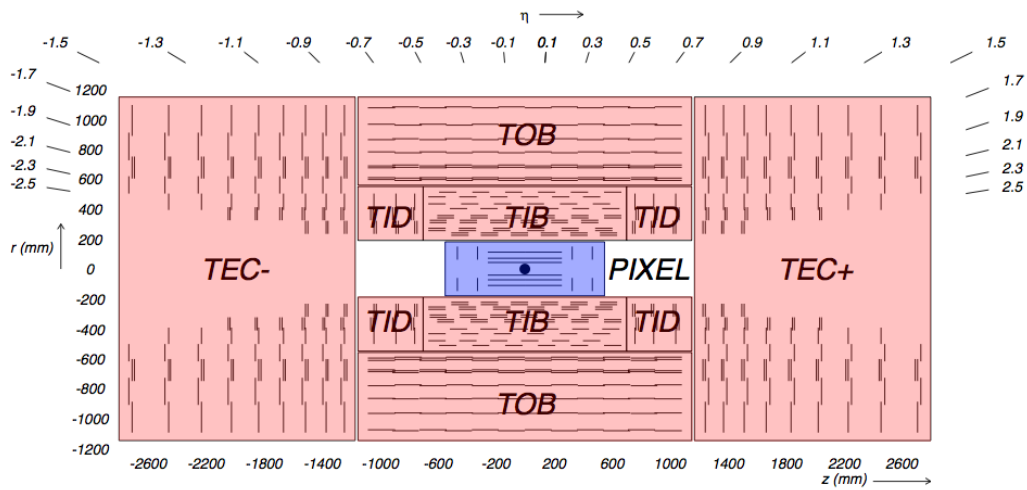


Figure 2-4: Schematic layout of tracker.

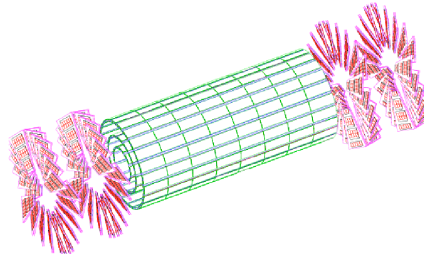


Figure 2-5: The pixel detector inside tracker.

<sup>142</sup>

<sup>143</sup> The pixel detector, though about the size of a shoebox, consists of 1440 segmented  
<sup>144</sup> silicon sensor modules with total 66 million readout channels. Charge carriers are  
<sup>145</sup> distributed over several pixels. The analog pulse height information can be used

146 to calculate the center of certain charge distribution which could improve the hit  
147 information. The spatial resolution is measured to be about  $10 \mu m$  for the  $r - \phi$   
148 plane or about  $20 \mu m$  for  $z$  direction measurement.

149 Outside the pixel detector, there comes the silicon strip detector. The barrel  
150 region of silicon strip detector is divided into two parts, the Tracker Inner Barrel  
151 (TIB) and the Tracker Outer Barrel (TOB). The former is composed of four layers  
152 of silicon sensors with a thickness of  $320 \mu m$  and of strip pitches varying from 80  
153 to  $120 \mu m$ . The TOB is made of six layers. In this kind of sub-detector, thicker  
154 silicon sensors ( $500 \mu m$ ) are employed, while the strip pitch varies from 120 to 180  
155  $\mu m$ . The endcap region ( $|\eta| > 1.6$ ) is covered by the Tracker Inner Disks (TID)  
156 and the Tracker End Cap (TEC). The entire silicon strip detector is comprised of  
157 15200 high-sensitivity modules consisting of detecting unit, supporting structure and  
158 readout electronic system.

### 159 2.2.2 ECAL

160 The Electromagnetic Calorimeter (ECAL) measures the energy of photons, electrons  
161 and positrons. It it is placed just outside the tracker, but still inside the solenoid.  
162 ECAL is made of 74848 lead-tungstate ( $PbWO_4$ ) crystals. This material is charac-  
163 terized by a high density ( $8.28 \text{ g/cm}^3$ ), which gives the crystals a very compact form  
164 and makes them particularly suitable to be placed inside the magnetic coil. Another  
165 reason, this material has also a fast temporal response ( $\sim 10 \text{ ns}$ ) and its radiation  
166 length ( $X_0$ ) of  $0.89 \text{ cm}$  give ECAL the possibility to fully contain the expansion of  
167 the electromagnetic shower.

168 The arrangement of ECAL is shown in Fig. (2-6). The barrel crystals have a front  
169 face area of  $2.2 \times 2.2 \text{ cm}^2$  and a length of 23 cm. They are positioned at  $r = 1.29$   
170 m in pseudo-rapidity region  $0 < |\eta| < 1.479$ . The crystals in the endcaps have a  
171  $2.47 \times 2.47 \text{ cm}^2$  front face, a 22 cm length and they are positioned at  $z = 3.17 \text{ m}$  in  
172  $1.479 < |\eta| < 3.0$ . A Preshower detector is placed in front of the endcaps crystals.  
173 The active elements of Preshower are two planes of silicon strips with a pitch of 1.9  
174 mm, which lie behind disks of lead absorber at depths of  $2X_0$  and  $3X_0$ . It allows the

175 rejection of photon pairs from  $\pi^0$  decays and improves the estimation of the direction  
176 of photons, to enhance the measurement of the two-photon invariant mass.

The energy resolution of the ECAL is given by three different contributions [19]  
(E in GeV),

$$\frac{\sigma_E}{E} = \frac{2.8\%}{\sqrt{E}} \oplus \frac{12\%}{E} \oplus 0.3\% \quad (2.1)$$

177 where the first term is statistical in nature, it also contains fluctuation in showering  
178 and in the amplification through photodiodes, the second one considers electronic  
179 noise and pile-up, the last term is mainly due to the calibration.

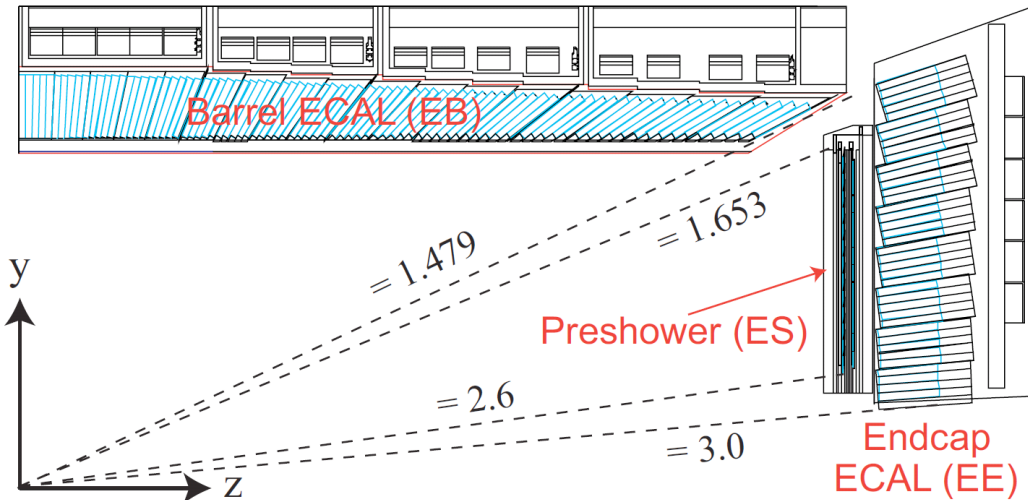


Figure 2-6: Schematic layout of the CMS ECAL.

### 180 2.2.3 HCAL

181 The hadron calorimeter (HCAL) is placed mainly between ECAL and the magnet  
182 coil. It measures the energy of hadrons and mesons. Additionally it provides indirect  
183 measurement of the presence of non-interacting, uncharged particles such as neutrinos.  
184 The design is strongly influenced by these aims, hence an important requirement is the  
185 high hermeticity (the ability to capture every particle emerging from the collisions).  
186 This means the detector must cover the biggest possible portion of the solid angle.

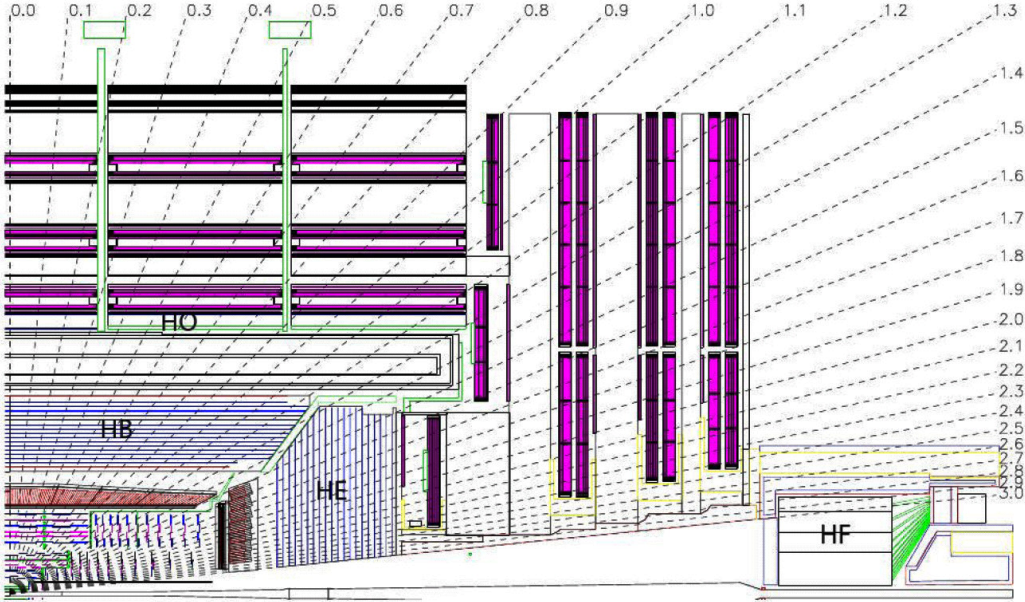


Figure 2-7: Longitudinal view of one quarter of CMS and the location of HB (hadron barrel calorimeter), HE (hadron endcap calorimeter), HF (hadron forward calorimeter) and HO (hadron outer calorimeter)

187 For this reason, a hadron forward calorimeter is required, which is placed outside  
 188 the magnet return yokes, with a total coverage of  $3 < |\eta| < 5.31$  at 11 m from the  
 189 interaction point. Moreover, an outer hadronic calorimeter is placed in the first muon  
 190 absorber layer in order to enhance the containment of high energy jets in the central  
 191 region of the detector.

192 HCAL is a sampling calorimeter, whose active elements are plastic scintillators  
 193 interleaved with brass absorber plates and read out by wavelength shifting fibers.  
 194 Brass has been chosen as absorber material for its short interaction length and because  
 195 it is non-magnetic. The thickness of the absorber layers is between 60 mm in the barrel  
 196 and 80 mm in the endcaps. The barrel has 5.46 interaction lengths at  $\eta = 0$  and 10.82  
 197 at  $\eta = 1.3$ , while the endcaps have an average of 11 interaction lengths [20].

The HCAL energy resolution ( $E$  in GeV and measured by pion) [21] is

$$\frac{\sigma_E}{E} \simeq \frac{a}{\sqrt{E}} \oplus 5\% \quad (2.2)$$

198 where  $a \simeq 65\%$  in the barrel,  $a \simeq 85\%$  in the endcaps and  $a \simeq 100\%$  in the HF.

199 **2.2.4 Muon Chamber**

200 The efficient detection of muons has primary importance, as muons represent a clear  
201 signature for a large number of processes. Muons can penetrate several meters of  
202 iron without interacting. Unlike most particles, they are not stopped by any of  
203 calorimeters in CMS. Therefore, chambers to detect muons are placed at the very  
204 edge of the experiment where they are the only particles likely to register a signal.

205 The muon system fulfills three purposes, muon identification, momentum mea-  
206 surement and triggering. Three different types of gaseous detectors are used for CMS  
207 muon system depending on the requirements.

208 **Drift Tube**

209 The drift tube (DT) system measures muon positions in the barrel part of the detector.  
210 Each DT chamber, on average  $2\text{ m} \times 2.5\text{ m}$  in size, consists of 12 aluminium layers,  
211 arranged in three groups of four segmentations, each with up to 60 4-cm-wide tubes  
212 that contain a stretched wire within each gas volume. The middle group measures  
213 the coordinate along the direction parallel to the beam and the two outside groups  
214 measure the perpendicular coordinate.

215 **Cathod Strip Chamber**

216 In the two endcaps, where the muon flux and the residual inhomogeneous magnetic  
217 field are higher, cathode strip chambers (CSC) are used. CSC is composed of anode  
218 wires and cathod strips in the gas volume. The chambers are arranged in 4 disks  
219 perpendicular to the beam, and in concentric rings (3 rings in the innermost station,  
220 2 in the others) in each of the endcaps.

221 **Resistive Plate Chambers**

222 Resistive plate chambers (RPC) are fast gaseous detectors that provide a muon trigger  
223 system parallel with DTs and CSCs. Each RPC consists of two parallel plates, a

<sup>224</sup> positively charged anode and a negatively charged cathode, both made of a very high  
<sup>225</sup> resistivity plastic material and separated by a gas volume.

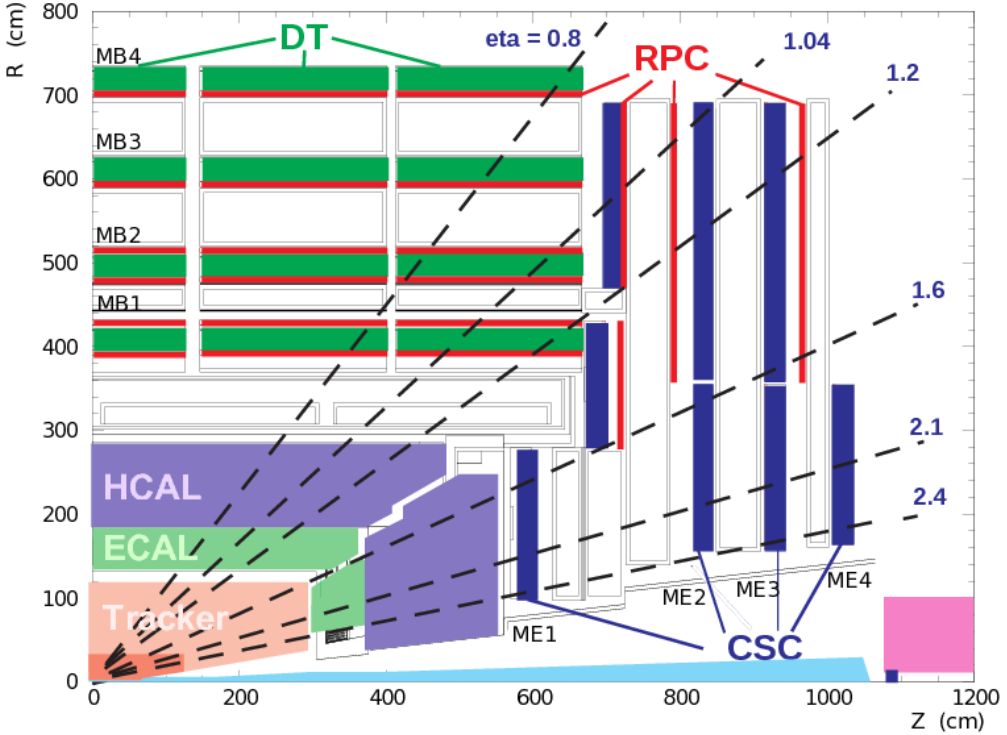


Figure 2-8: Slice view of one quarter of muon chamber system.

### <sup>226</sup> 2.2.5 Trigger System

<sup>227</sup> To have a good chance of producing rare particles, a very large number of collisions  
<sup>228</sup> is required (LHC proton bunches collide every 25 ns). Most collision events in the  
<sup>229</sup> detector are soft and do not produce interesting events. The amount of data from  
<sup>230</sup> each crossing is approximately 1 megabytes, which at the 40 MHz crossing rate would  
<sup>231</sup> result in 40 terabytes of data a second, an amount that the experiment cannot store.  
<sup>232</sup> The task of the trigger system is to reduce the storage rate while keeping a high  
<sup>233</sup> efficiency on the potentially interesting events. In CMS the input rate is reduced in  
<sup>234</sup> two steps, Level-1 Trigger (L1T) and High-Level Trigger (HLT).

235 **Level-1 Trigger**

236 After the Level-1 Trigger selection, the event recording frequency is decreased to  
237 100kHz [22], which is much smaller than the collision rate. The L1T objects are  
238 particles (such as photons, muons and electrons), jet candidates, global transverse  
239 energy and missing transverse energy. Level-1 Trigger just chooses the event with  $E_T$   
240 and  $P_T$  higher than the thresholds.

241 **High Level Trigger**

242 High Level Trigger is behind the readout buffers after Level-1 Trigger. It reduces  
243 the data output rate to 100Hz by using all the information from CMS including the  
244 sub-detectors. The reconstruction algorithms are the same as the off-line analysis.  
245 However, the triggering procedure doesn't need maximal precision, therefore these  
246 algorithms are modified to be faster even with lower resolution.

247

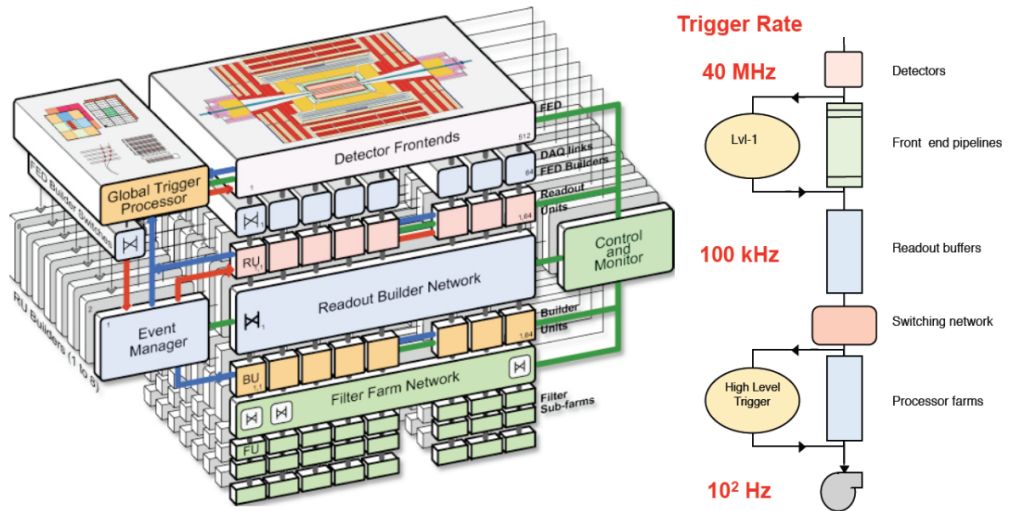


Figure 2-9: CMS triggering and data acquisition architecture.

248 **Chapter 3**

249 **Analysis Procedures**

250 In this chapter, the analysis procedures of the search for  $Z'$  decaying into  $Zh$  in  $llbb$   
251 final state are reported. The data sets and Monte Carlo (MC) samples we used in this  
252 analysis will be indicated. Physics objects reconstruction and event selections are also  
253 introduced. Moreover, background yields and the effects of systematic uncertainties  
254 will be demonstrated in the end of this chapter.

255 **3.1 Monte Carlo Samples and Data sets**

256 **3.1.1 Signal MC**

257 As introduced in section 1.2.3, the signal hypothesis is HVT model B benchmark.  
258 The heavy resonance ( $Z'$ ) is tested using a wide set of masses from 800 GeV to  
259 2000 GeV, one masspoint every 100 GeV (Table 3.1). The signal is simulated by  
260 MadGraph5\_aMC@NLO [23] in LO mode, as a narrow spin-1 neutral resonance and  
261 is forced to decay in the  $Z' \rightarrow Zh \rightarrow llqq$  channel. Showering and hadronization are  
262 performed with PYTHIA6 [24].

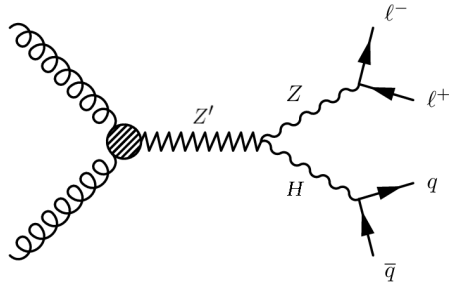


Figure 3-1: Feynman diagram for  $Z' \rightarrow Zh \rightarrow 2l2q$ .

Sample	Number of Processed Events	$\sigma_{LO}(\text{pb})$
ZPrime_ZH_lljj_M800-MADGRAPH	10710	0.00685367
ZPrime_ZH_lljj_M900-MADGRAPH	10209	0.00485861
ZPrime_ZH_lljj_M1000-MADGRAPH	19997	0.003263
ZPrime_ZH_lljj_M1100-MADGRAPH	9370	0.00217483
ZPrime_ZH_lljj_M1200-MADGRAPH	10710	0.00145484
ZPrime_ZH_lljj_M1300-MADGRAPH	9369	0.000979745
ZPrime_ZH_lljj_M1400-MADGRAPH	10497	0.000664783
ZPrime_ZH_lljj_M1500-MADGRAPH	19999	0.000454339
ZPrime_ZH_lljj_M1600-MADGRAPH	8950	0.000312541
ZPrime_ZH_lljj_M1700-MADGRAPH	9369	0.000216282
ZPrime_ZH_lljj_M1800-MADGRAPH	10708	0.000150398
ZPrime_ZH_lljj_M1900-MADGRAPH	10498	0.000105039
ZPrime_ZH_lljj_M2000-MADGRAPH	19999	7.36377e-05

Table 3.1: Signal samples used in the analysis.

263 **3.1.2 Background MC**

264 Since we are looking for new resonances decaying in semi-leptonic final state, the  
265 background samples of this analysis are originated by all SM events with two leptons  
266 and at least one jet as final state. The dominant background contribution is the  
267 production of Z boson with jets. This Z+jets sample is produced by MADGRAPH.  
268 In the matrix element level, the Z boson is forced decaying into two leptons, and  
269 further this sample is divided into two samples depending on the Z  $p_T$ , higher than  
270 100 GeV or between 70 and 100 GeV. The contribution of events with Z  $p_T$  less than  
271 70 GeV is negligible due to further cut on the objects  $p_T$  in the selection criteria.

272 The second dominant source of background is  $t\bar{t}$  production. Both of the two top  
273 quarks decay into all leptonic final state (top decays into a W boson and a b quark  
274 first) which gives two leptons, neutrinos and two b-jets. This sample is generated by  
275 POWHEG [25].

276 Other sources of background considered are SM di-boson productions (WW, WZ  
277 and ZZ) generated by PYTHIA6. All the background samples are required to pass  
278 phase-space cuts,  $p_T^l > 60$  GeV and  $60 < M_{ll} < 120$  GeV. Related statistics are reported  
279 in Table 3.2.

Sample	Number of Processed Events	$\sigma_{NLO}(\text{pb})$
DYJetsToLL_PtZ-70To100	11764538	63.5
DYJetsToLL_PtZ-100	12511326	39.4
TTTo2L2Nu2B	10783509	25.8
WW	7759752	$56.0 \pm 2.3 (\pm 0.3)$
WZ	9910267	22.4
ZZ	9769891	$7.6 \pm 0.3 (\pm 0.3)$

Table 3.2: Background samples used in the analysis.

280 **3.1.3 Data Samples**

281 In this analysis, the full CMS data collected in 2012 is used, corresponding to the  
282 integrated luminosity of  $19.7 \text{ fb}^{-1}$  at center-of-mass energy  $\sqrt{s} = 8$  TeV. For each  
283 lepton channel, there are four datasets. All datasets are collected with a double

muon or a double electron trigger, as explained in detail in the next section. The trigger algorithm employed for the electron samples doesn't use any information from the tracker but only the energy deposite in the ECAL. This expedient is implemented in order to avoid any possible inefficiencies due to the presence of two tracks very close to each other when the Z is highly boosted and its decay products are very collimated. Such a trigger is contained in the Photon/DoublePhotonHighPt dataset.  
 The full dataset names are listed in Table 3.3.

AOD Sample	Luminosity ( $\text{pb}^{-1}$ )
DoubleMu/Run2012A-22Jan2013-v1	876.225
DoubleMuParked/Run2012B-22Jan2013-v1	4409
DoubleMuParked/Run2012C-22Jan2013-v1	7017
DoubleMuParked/Run2012D-22Jan2013-v1	7369
Photon/Run2012A-22Jan2013-v1	876.225
DoublePhotonHighPt/Run2012B-22Jan2013-v1	4412
DoublePhotonHighPt/Run2012C-22Jan2013-v1	7055
DoublePhotonHighPt/Run2012D-22Jan2013-v1	7369

Table 3.3: Data sets used in this analysis.

## 3.2 Trigger

Since the final state contains two same flavour leptons and at least one jet, we perform this analysis on the DoubleMu and Photon/DoublePhotonHighPt datasets. The first dataset is triggered by two muons, the second one is triggered by two eletrons. These triggers are:

- HLT\_Mu22\_TkMu8\* (for DoubleMu datasets)
- HLT\_DoubleEle33\_\*(for Photon/DoublePhontonHighPt datasets)

The muon trigger has a double  $p_T$  threshold, requires leading muon  $p_T$  greater than 22 GeV and sub-leading muon  $p_T$  greater than 8 GeV. Differently, the double electron trigger requires a higher threshold of 33 GeV to electrons. The trigger efficiencies are close to 1 in both cases.

302    **3.3 Physics Objects**

303    **3.3.1 Muon**

304    **Reconstruction**

305    The muon reconstruction algorithm at CMS takes advantage of the redundancy of  
306    detection methods. Muon tracks are first reconstructed independently in the inner  
307    tracker (tracker track) and in the muon system (standalone track). Based on these  
308    objects, two reconstruction approaches are used [26]:

309       • *Globol Muon* (outside-in): Starting from a standalone track, this algorithm  
310       finds a best tracker track to match the standalone track. Then, the fit of the  
311       track is repeated using the hits both in the tracker and in the muon system [27].  
312       The resulting object is called a *Global Muon*. At large transverse momentum  
313       ( $p_t > 200$  GeV), the global muon fit can improve the momentum resolution  
314       compared to the tracker only fit.

315       • *Tracker Muon* (inside-out): A tracker muon is reconstructed by an opposite  
316       direction from a global muon. In this approach, all tracker tracks with  $p_T >$   
317       0.5 GeV and the total momentum  $p > 2.5$  GeV are considered as possible  
318       muon candidates. The extrapolation to the muon system takes into account the  
319       magnetic field, average expected energy losses, and multiple scattering in the  
320       detector material. If at least one muon segment matches the extrapolated track,  
321       the corresponding track track qualifies as a *Tracker Muon*. This algorithm is  
322       useful for low- $p_T$  muons that are not fully penetrate the muon system, and  
323       therefore only register a few hits

324       If no match is found when extrapolating outside-in, the standalone track is stored  
325       as a *Stanalone Muon*. This happens only for less than 1% of the muons produced in  
326       a collison, and the reconstruction efficiency is about 99% for the muon which carries  
327       enough high momentum within detector coverage [26].

328    **Identification**

329    We use both tracker muons and global muons in this analysis. To identify muons  
330    from the signal, the muons must pass one of these two off-line selections, high- $p_T$   
331    muon ID or tracker-based muon ID [28]. The requirements are listed as follows:

332

333    High- $p_T$  muon ID

334       • Muon identified as a *Global Muon*.

335       • Number of muon hits in the global track  $> 0$ .

336       • Number of matched muon stations  $> 1$ .

337       • Number of pixel hits  $> 0$ .

338       • Number of tracker layer with hits  $> 8$ .

339       • Transverse impact parameter  $d_{xy} < 0.2$  cm.

340       • Longitudinal impact parameter  $d_z < 0.5$  cm.

341       • Relative error on the track transverse momentum  $\sigma_{p_T}/p_T < 0.3$ .

342

343    In the tracker-based muon ID, the muon has to be identified as a *Tracker Muon*,  
344    and the requirement of muon hits in the global track is removed. Other requirements  
345    are the same.

346    An additional useful variable for lepton identification is the isolation. It is defined  
347    as the scalar sum of the  $p_T$  of the reconstructed objects within a cone (typical size  
348    is  $\Delta R = 0.3$ ) space around the lepton track but excluding the  $p_T$  of the lepton  
349    itself. Moreover, the relative isolation is defined as isolation divided by the lepton  
350     $p_T$  ( $I_{rel} = Iso/p_T^{lept}$ ). The relative isolation is more frequently used in the modern  
351    analysis.

352    In this analysis, a modified isolation criteria is used. The two muons originated  
353    from boosted Z decay are close to each other, and consequently the presence of another

354 muon in the isolation cone could break the function of this variable. In order to solve  
 355 this problem we use a tracker-based isolation relative quantity, explicitely removing  
 356 the momentum flow from any other muon passing our muon selection. Moreover, a  
 357 tracker-based isolation is well motivated also by two additional aspects: it is more  
 358 independent of pile up (pile-up tracks tipically do not match the primary vertex)  
 359 and does not include possible muon radiation. Finally, the modified requirement is  
 360  $I_{rel}^{mod} < 0.1$ .

361

Variable	High- $p_T$	Tracker-based
Muon type	Global muon	Tracker muon
Muon hits in global track	$\geq 1$	-
Muon stations matched	$\geq 2$	$\geq 2$
$d_{xy}$	$< 0.2$ cm	$< 0.2$ cm
$d_z$	$< 0.5$ cm	$< 0.5$ cm
Pixel hits	$\geq 1$	$\geq 1$
Tracker layers	$\geq 8$	$\geq 8$
$\sigma_{p_T}/p_T$	$< 0.3$	$< 0.3$
$I_{rel}^{mod}$	$< 0.1$	$< 0.1$

Table 3.4: Summary of the muon ID selection criteria.

362 **3.3.2 Electron**

363 **Reconstruction**

364 Electrons are reconstructed from energy deposits in the ECAL matched to tracks  
365 reconstructed in the silicon tracker. They have less distinguishable signatures than  
366 muons in the detector due to the jet induced background in ECAL. Therefore, to  
367 reconstruct an election, it's essential to find a brilliant way to match the infomation  
368 acquired in both tracker and ECAL.

369 **Clustering**

370 For every single hit from an electron in ECAL, approximately 94% of energy is con-  
371 tained in  $3 \times 3$  crystals and 97% in  $5 \times 5$  crystals. To form a cluster, crystals with  
372  $E_T > 1$  GeV is picked as seeds. Then starting from seed crystal, dominos of size  $1 \times 3$   
373 or  $1 \times 5$  are created in  $\eta - \phi$  plane. If the energy of these dominos exceed 0.1 GeV  
374 threshold, thus added up the energy of dominos along the  $\phi$  direction.

375 Moreover, the effects of conversion process and bremsstrahlung radiation must be  
376 taken into account to reconstruct the electron energy more precisely. The concept  
377 of electron superclustering is to collect the energy of photons from bremsstrahlung  
378 radiation along the  $\phi$  direction with fixed  $\eta$  width of the seed crystal. The technical  
379 details of the supercluster can be found in [29].

380 **Tracking**

381 There are several steps to reconstruct electron tracks in CMS experiment. The hit  
382 on the pixel and the tracker are reconstructed in the first step. The second step is  
383 to find the seed of tracks by matching at least two hits in pixel detector. Lst step  
384 is to fit the trajetory starting from the seed. To perform this fit, the Gaussian-sum  
385 filter (GSF) algorithm is used [30]. In GSF algorithm, the energy loss probability  
386 density function is constructed by multiple Gaussian functions. Finally, the electrons  
387 are built by matching the superclusters to the GSF tracks. Reconstruction efficiencies

388 for electrons  $E_T > 20$  GeV are generally above 95% in EB and 90% in EE [31].

## 389 Identification

390 The electron identification used in this analysis is based on HEEPv4.1 [32]. As what  
391 we did for the muon id, we need to modify the isolation definition again because of  
392 the small  $\Delta R$  between two electrons. The requirements are listed as follows:

393

394 Modified HEEPv4.1 electron ID

- 395 • Transversal supercluster energy  $> 35$  GeV.
- 396 • Pseudorapidity of supercluster  $\eta_{SC} < 1.442$  for barrel electrons, or  $1.56 < \eta_{SC} <$   
397 2.5 for endcap electrons.
- 398 • Have either  $E_{2\times 5}/E_{5\times 5} > 0.94$  or  $E_{1\times 5}/E_{5\times 5} > 0.83$ .

399 • Ratio of HCAL deposit energy to ECAL deposit energy (Fig. 3-2) smaller than  
400 0.5.

- 401 • Number of inner layer lost hits smaller than 2.
- 402 • Have  $d_{xy} < 0.02$  cm for barrel electrons, or  $d_{xy} < 0.05$  cm for endcap electrons.

403

404 As what we did for the muon id, by the same reason we need to modify the  
405 isolation definition again. In this case there are three isolation variables have to be  
406 changed.

- 407 • Modified track isolation is required to lower than 5 GeV. This variable is defined  
408 as the scalar  $p_T$  sum of the tracks within a  $\Delta R = 0.3$  cone around the electron,  
409 and excluding the  $p_T$  of another electron which passes the above selections and  
410 its track is inside the cone.

- 411 • The electromagnetic calorimeter isolation  $I_{ECAL}$  is defined as the scalar sum of  
412  $E_T$  of the crystals in a  $\Delta R = 0.3$  cone around the particular electron (an inner

area of full-width 3 crystal), excluding a 4 crystals  $\Delta R$  cone around any other electron. The dimension of the ECAL crystals corresponds roughly at  $\Delta R \sim 0.01$  to 0.02. The threshold of  $I_{ECAL}$  is varying with the electron transverse energy.

- The hadronic calorimeter isolation  $I_{HCAL}$  is defined as the scalar sum of  $E_T$  of the HCAL caloTowers with a center in a  $\Delta R = 0.3$  cone around the electron, excluding those lying within  $\Delta R = 0.15$  of the electron itself and of any other electron [33]. The threshold of this variable also varies with the electron transverse energy.

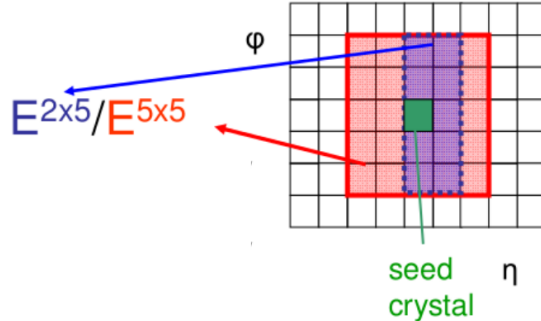


Figure 3-2: Example of the  $E_{2\times 5}/E_{5\times 5}$  computation in the ECAL crystals.  $E_{i\times j}$  is the energy contained in a  $i \times j$  block around the seed crystal (defined as the highest deposit of the energy of the cluster).

Variable	Barrel	Endcap
$E_T$	$> 35 \text{ GeV}$	$> 35 \text{ GeV}$
$ \eta_{SC} $	$ \eta_{SC}  < 1.442$	$1.56 <  \eta_{SC}  < 2.5$
H/E	$< 0.05$	$< 0.05$
$E_{2\times 5}/E_{5\times 5}$	$> 0.94$ or $E_{1\times 5}/E_{5\times 5} > 0.83$	-
Inner Layer Lost Hits	$<= 1$	$<= 1$
$ d_{xy} $	$< 0.02 \text{ cm}$	$< 0.05 \text{ cm}$
$Iso_{Trk}^{mod}$	$< 5 \text{ GeV}$	$< 5 \text{ GeV}$
$Iso_{Ecal,Hcal}^{mod}$	$< 2 \text{ GeV} + 0.03E_T$	$< 2.5 \text{ GeV for } E_T < 50 \text{ GeV}$ $< 2.5 \text{ GeV} + 0.03E_T \text{ for } E_T > 50 \text{ GeV}$

Table 3.5: Summary of the modified HEEPV4.1 electron ID.

422 **3.3.3 Jet**

423 Since gluons and quarks cannot exist in free state due to the color confinement  
424 [34], they fragment into hadrons. The result of this fragmentation (or called the  
425 "hadronization") is a jet of particles depositing energy in the detectors.

426 **Reconstruction**

427 Jet clustering algorithms are among the main tools for analyzing data from hadronic  
428 collisions. In this section, a extensively used clustering algorithm called "sequential  
429 recombination algorithm" [35,36] will be introduced. At first, events are reconstructed  
430 using the particle flow algorithm (PF) [37], which attempts to identify and measure all  
431 the stable particles in a collision by combining information from all the sub-detectors.  
432 The PF algorithm categorizes all particles into five types: muons, electrons, photons,  
433 charged and neutral hadrons. The resulting particle flow candidates are passed to  
434 the anti- $k_T$  (AK) [35] or Cambridge/Aachen (CA) [36,38] jet clustering algorithms to  
435 create jets (AK and CA are two commonly used branches of sequential recombination  
436 algorithms).

437 The jet clustering algorithms are implemented as follows:

$$d_{iB} = p_{T,i}^{2p}$$
$$d_{ij} = \min(p_{T,i}^{2p}, p_{T,j}^{2p}) \frac{\Delta R_{i,j}^2}{R^2} \quad (3.1)$$

438 In Eq. (3.1), the pair of objects ( i , j ) denote two input candidate particles to  
439 the algorithm.  $\Delta R_{i,j}$  is the spatial distance between the two objects, and  $R$  is the  
440 typical cone size of the jet. The parameter  $p$  corresponds to different catagories of  
441 algorithms and will be introduced in the later paragraph.

442 The clustering proceeds by comparing the value of the two quantities,  $d_{iB}$  and  $d_{ij}$ .  
443 If  $d_{ij} > d_{iB}$ , the algorithm will look for another possible combination of ( i , j ). If  
444  $d_{ij} < d_{iB}$ , the 4-momentum of object i will merge into j, and then the object j forms a

445 pseudo-jet, but the algorithm will not stop looking for a new object until all particles  
446 are clustered into jet.

447 The parameter  $p$  can be chosen as follows:

448 •  $p = 0$  : Cambridge/Aachen algorithm;

449 •  $p = -1$  : Anti- $k_T$  algorithm;

450 The difference between CA/AK algorithms is clear, CA algorithm is only consid-  
451 ering the spatial distance of the two candidate objects (if  $\Delta R_{ij} < R$ , merged). In the  
452 case of anti- $k_T$  algorithm,  $p_T$  of the object presents as a weight for the distance.

453 The anti- $k_T$  algorithm have better energy calibration, while the CA algorithm  
454 was found to be more efficient at finding hard subjets within the jets in simulation-  
455 based studies [39]. Therefore the CA jets are used in this analysis to identify events  
456 containing hadronically-decaying Higgs bosons.

## 457 Identification

458 As discussed in the previous section, this analysis use the Cambridge/Aachen algo-  
459 rithm with a cone radius of  $R = 0.8$  for the identification of jets (CA8 jets). Further-  
460 more, jets are required to pass the following loose identification criteria [40, 41]:

461

462 Loose JetID ( $> 99\%$  efficiency)

463 • Muon energy fraction smaller than 0.99

464 • Photon energy fraction smaller than 0.99

465 • Charged electromagnetic energy fraction smaller than 0.99

466 • Neutral hadron energy fraction smaller than 0.99

467 • Charged hadron energy fraction larger than 0

468 • Number of constituent particles larger than 1

469      For the "charged" variables,  $\eta < 2.4$  requirement are also applied, since there is  
470 no track coverage outside of this region, whereas the "neutral" variables extend to  
471 the whole  $\eta$  region.

472 **3.3.4 Jet Grooming Algorithms and Pruned Jet Mass**

473 The jet mass is the main observable in distinguishing a boson-jet from a QCD jet. Jet  
474 grooming aims to suppress uncorrelated underlying events and pile-up radiation from  
475 the target jet, and improves the discrimination by pushing the jet mass for QCD  
476 jets towards lower values while maintaining the jet mass for boson-jets around the  
477 boson-mass [42, 43].

# 478 Bibliography

- 479 [1] ATLAS Collaboration. Observation of a new particle in the search for the Stan-  
480 dard Model Higgs boson with the ATLAS detector at the LHC. *Phy. Lett. B*,  
481 716:1, 2012.
- 482 [2] CMS Collaboration. Observation of a new boson at a mass of 125 GeV with the  
483 CMS experiment at the LHC. *Phy. Lett. B*, 716:30, 2012.
- 484 [3] CMS Collaboration. Observation of a new boson with mass near 125 GeV in pp  
485 collisions at  $\sqrt{s} = 7$  and 8 TeV. *JHEP*, 06:081, 2013.
- 486 [4] CMS Collaboration. Precise determination of the mass of the Higgs boson and  
487 tests of compatibility of its couplings with the standard model predictions using  
488 proton collisions at 7 and 8 TeV. *Eur. Phys. J. C*, 75:212, 2015.
- 489 [5] ATLAS Collaboration. Measurement of the Higgs boson mass from the  $H \rightarrow \gamma\gamma$   
490 and  $H \rightarrow ZZ^* \rightarrow 4l$  channels in pp collisions at center-of-mass energies of 7 and  
491 8 TeV with the ATLAS detector. *Phys. Rev. D*, 90:052004, 2014.
- 492 [6] ATLAS Collaboration. Evidence for the spin-0 nature of the Higgs boson using  
493 ATLAS data. *Phys. Lett. B*, 726:120, 2013.
- 494 [7] CMS and ATLAS Collaboration. Combined Measurement of the Higgs Boson  
495 Mass in pp Collisions at  $\sqrt{s} = 7$  and 8 TeV with the ATLAS and CMS Experi-  
496 ments. *Phys. Rev. Lett.*, 114:191803, 2015.
- 497 [8] Mads T. Frandsen. Minimal Walking Technicolor. arXiv:0710.4333 [hep-ph],  
498 <http://arxiv.org/abs/0710.4333>, 2007.
- 499 [9] T. Han, H. E. Logan, B. McElrath, and L.-T. Wang. Phenomenology of the little  
500 Higgs model. *Phys. Rev. D*, 67:095004, 2003.
- 501 [10] M. Schmaltz and D. Tucker-Smith. LITTLE HIGGS THEORIES. *Annual Review*  
502 *of Nuclear and Particle Science*, 55:no. 1, 229–270, 2005.
- 503 [11] M. Perelstein. Little Higgs models and their phenomenolog. *Progress in Particle*  
504 *and Neclear Physics*, 58:no. 1, 247–291, 2007.
- 505 [12] R. Contino, D. Pappadopulo, D. Marzocca, and R. Rattazzi. On the effect of  
506 resonances in composite Higgs phenomenology. *Journal of High Energy Physic*,  
507 2011:no. 10, 1–50, 2011.

- 508 [13] D. Marzocca, M. Serone, and J. Shu. General composite Higgs model. *Journal*  
 509 *of High Energy Physics*, 2012:no. 8, 1–52, 2012.
- 510 [14] B. Bellazzini, C. Csaki, and J. Serra. Composite Higgses. *Eur. Phys. J.*, C74:no.  
 511 5, 2766, 2014.
- 512 [15] D. Pappadopulo, R. Torre A. Thamm, and A. Wulzer. Heavy vector triplets:  
 513 bridging theory and data. *Journal of High Energy Physics*, 2014:no. 9, 1–50,  
 514 2014.
- 515 [16] Andrea Wulzer. An Equivalent Gauge and the Equivalence Theorem.  
 516 arXiv:1309.6055 [hep-ph], <http://arxiv.org/abs/1309.6055>, 2013.
- 517 [17] V. Barger, W.-Y. Keung, and E. Ma. Gauge model with light W and Z bosons.  
 518 *Phys. Rev. D*, 22:727, 1980.
- 519 [18] Lisa Benato, Yu-Hsiang Chang, Ching-Wei Chen, Michele de Gruttola, Ra-  
 520 man Khurana Ji-Kong Huang, Stefano Lacaprara, Yun-Ju Lu, Jacopo Pazzini,  
 521 Maurizio Pierini, Henry Yee-Shian Tong, Jun-Yi Wu, Shin-Shan Eiko Yu, Marco  
 522 Zanetti, and Alberto Zucchetta. Search for heavy resonances decaying into a vec-  
 523 tor boson and a Higgs boson in the  $(ll, l\nu, \nu\nu)b\bar{b}$  final state. CMS Note 2015/186,  
 524 CMS, 2015.
- 525 [19] A. Benaglia. The CMS ECAL performance with examples. *JINST*, 09:C02008,  
 526 2014.
- 527 [20] CMS HCAL Collaboration. Design, Performance, and Calibration of CMS  
 528 Hadron-Barrel Calorimeter Wedges. CMS Note 2006/138, CMS, 2006.
- 529 [21] Victor Daniel Elvira. Measurement of the Pion Energy Response and Resolution  
 530 in the CMS HCAL Test Beam 2002 Experiment. CMS Note 2004/020, CMS,  
 531 2004.
- 532 [22] J. Brooke on behalf of the CMS Collaboration. Performance of the CMS Level-1  
 533 Trigger. arXiv:1302.2469 [hep-ex], <http://arxiv.org/abs/1302.2469>, 2013.
- 534 [23] J. Alwall, R. Frederix, S. Frixione, V. Hirschi, F. Maltoni, O. Mattelaer, H.-S.  
 535 Shaoand T. Stelzer, P. Torrielli, and M. Zaro. The automated computation of  
 536 tree-level and next-to-leading order differential cross sections, and their matching  
 537 to parton shower simulations. *JHEP*, 07:079, 2014.
- 538 [24] Torbjorn Sjostrand, Stephen Mrenna, and Peter Skands. PYTHIA 6.4 Physics  
 539 and Manual. *JHEP*, 0605:026, 2006.
- 540 [25] Stefano Frixione, Paolo Nason, and Giovanni Ridolfi. The POWHEG-hvq manual  
 541 version 1.0. arXiv:0707.3081 [hep-ph], <http://arxiv.org/abs/0707.3081>, 2007.
- 542 [26] S. Chatrchyan et al. Performance of CMS muon reconstruction in pp collision  
 543 events at  $\sqrt{s} = 7$  TeV. *JINST*, 7:P10002, 2012.

- 544 [27] Wolfgang Adam, Boris Mangano, Thomas Speer, and Teddy Todorow. Track  
 545 Reconstruction in the CMS tracker. CMS Note 2006/041, CMS, 2006.
- 546 [28] CMS Collaboration. Baseline muon selections for Run-I.  
 547 <https://twiki.cern.ch/twiki/bin/view/CMSPublic/SWGuideMuonId>.
- 548 [29] CMS Collaboration. Physics TDR volume I, The CMS Physics Technical Design  
 549 R I. CERN-LHCC-2006-001, page 521pp, 2006.
- 550 [30] W. Adam, R. Frhwirth, A. Strandlie, and T. Todorov. Reconstruction of elec-  
 551 trons with the gaussian-sum filter in the cms tracker at the lhc. *Journal of*  
 552 *Physics G: Nuclear and Particle Physics*, 31(9):N9, 2005.
- 553 [31] CMS Collaboration. E/gamma Commissioning and physics deliverables.  
 554 <https://twiki.cern.ch/twiki/bin/view/CMS/EgCommissioningAndPhysicsDeliverables>.
- 555 [32] CMS Collaboration. HEEP Electron ID and isolation.  
 556 <https://twiki.cern.ch/twiki/bin/viewauth/CMS/HEEPElectronID>.
- 557 [33] T. S. Williams, D. Newbold, and C. Shepherd-Themistocleous. Modified isolation  
 558 cuts for the selection of high  $p_T$  electrons from the decay of boosted Z bosons.  
 559 CMS Note 2012/168, CMS, 2012.
- 560 [34] Wikipedia. Color confinement. [https://en.wikipedia.org/wiki/Color\\_confinement](https://en.wikipedia.org/wiki/Color_confinement).
- 561 [35] M. Cacciari, G. P. Salam, and G. Soyez. The anti- $k_t$  jet clustering algorithm.  
 562 *JHEP*, 04:063, 2008.
- 563 [36] M. Wobisch and T. Wengler. Hadronization corrections to jet cross section in  
 564 deep-inelastic scattering. arXiv:9907280 [hep-ph], <http://arxiv.org/abs/9907280>,  
 565 1999.
- 566 [37] CMS Collaboration. Commissioning of the Particle-Flow reconstruction in  
 567 Minimum-Bias and Jet Events from pp Collisions at 7 TeV. CMS Physics Anal-  
 568 ysis Summary CMS-PAS-PFT-10-002, CMS, 2010.
- 569 [38] Y.L. Dokshitzer et al. Better jet clustering algorithms. *JHEP*, 08:001, 1997.
- 570 [39] CMS Collaboration. A Cambridge-Aachen (C-A) based Jet Algorithm for  
 571 boosted top-jet tagging. CMS Physics Analysis Summary CMS-PAS-JME-09-  
 572 001, CMS, 2009.
- 573 [40] N.Saoulidou and E.Tziaferi. Performance of the Particle-Flow jet identification  
 574 criteria using proton-proton collisions at = 8 TeV. CMS Note 2014/227, CMS,  
 575 2014.
- 576 [41] CMS Collaboration. Jet Identification. <https://twiki.cern.ch/twiki/bin/viewauth/CMS/JetID>.
- 577 [42] P. Tran et al. Measurement of jet mass in V+Jets events. CMS Note 2012/137,  
 578 CMS, 2012.

- <sup>579</sup> [43] A. Bonato, R. Gerosa, and et al. Identifying hadronically decaying W bosons  
<sup>580</sup> merged into a single jet. CMS Note 2013/072, CMS, 2013.